npj | computational materials

www.nature.com/npjcompumats

ARTICLE OPEN

Emergent topological states via digital (001) oxide superlattices

Zhiwei Liu[1,2,3,7], Hongquan Liu[2,7], Jiaji Ma[2], Xiaoxuan Wang[2], Gang Li[4,5] ✉ and Hanghui Chen[2,3,6] ✉

Oxide heterostructures exhibit many intriguing properties. Here we provide design principles for inducing multiple topological states in (001) $(AMO_3)_1/(AM'O_3)_1$ oxide superlattices. Aided by first-principles calculations and model analysis, we show that a $(SrMO_3)_1/(SrM'O_3)_1$ superlattice ($M = $ Nb, Ta and $M' = $ Rh, Ir) is a strong topological insulator with Z_2 index (1;001). More remarkably, a $(SrMoO_3)_1/(SrIrO_3)_1$ superlattice exhibits multiple coexisting topological insulator (TI) and topological Dirac semi-metal (TDS) states. The TDS state has a pair of type-II Dirac points near the Fermi level and symmetry-protected Dirac node lines. The surface TDS Dirac cone is sandwiched by two surface TI Dirac cones in the energy-momentum space. The non-trivial topological properties arise from the band inversion between *d* orbitals of two dissimilar transition metal atoms and a particular parity property of (001) superlattice geometry. Our work demonstrates how to induce non-trivial topological states in (001) perovskite oxide heterostructures by rational design.

npj Computational Materials (2022)8:208 ; https://doi.org/10.1038/s41524-022-00894-5

INTRODUCTION

Complex oxides exhibit a wide range of intriguing phenomena such as Mott insulators[1–3], long-range charge/spin/orbital orders[4–6], multiferroics[7–12], and high-temperature superconductivity[13–17]. On the other hand, searching for non-trivial topological states in solid-state[18,19], photonic[20,21] and acoustic[22,23] crystals has been one of the most active fields in condensed matter physics and materials science. In time-reversal-invariant crystalline solids, topological insulating state and topological metallic state (with Dirac points and/or Dirac node lines) have been intensively studied in narrow-gap semiconductors whose electronic structure is dominated by *s* and *p* orbitals[24–32]. In comparison, complex oxides with characteristic *d* orbitals have been less explored. Previous studies propose that bulk $YiBiO_3$[33] and electron doped $BaBiO_3$[34] are candidates for topological insulators, in both of which a *s-p* band inversion occurs and spin-orbit coupling opens a gap, similar to Bi_2Se_3[30]. Crystal symmetry (in particular with non-symmorphic space group) has been exploited to search for Dirac points and Dirac node lines in non-magnetic oxides such as $SrNbO_3$[35] and $SrIrO_3$[36,37]. Recently, high-mobility and giant magnetoresistance have been observed in Dirac semi-metal $CaIrO_3$[38,39].

The advances in thin-film deposition techniques enable the synthesis of digital oxide superlattices and heterostructures, providing a different approach to inducing non-trivial topological states in complex oxides[40–42]. In particular, oxide superlattices or heterostructures can furnish artificially engineered electronic structure that is lacking in bulk[43,44]. An intriguing proposal is to study a bi-layer of perovskite oxide AMO_3 thin film along (111) direction[45,46], in which the transition metal atom *M* resides on a buckled honeycomb lattice. The transition metal *d*-bands generically form a linear crossing at the high-symmetry *K* point in the Brillouin zone and spin-orbit coupling (SOC) opens a gap at the crossing[47] and thus non-trivial topological states may emerge such as quantum spin Hall state[48,49]. When local interactions are considered, other more exotic topological states such as quantum anomalous Hall and fraction quantum Hall states are also possible[50–52]. However, (111) terminations of perovskite oxide AMO_3 are polar and it is very difficult to synthesize such films with a precise control of their thickness in experiment[46]. By contrast, (001) perovskite oxide heterostructures have been routinely synthesized[53,54], in particular those oxides with non-polar terminations $[A^{2+}O^{2-}]$ and $[M^{4+}(O^{2-})_2]$. They can be accurately controlled on the atomic scale in a layer-by-layer manner in an oxide superlattice[55].

In this work, we provide a different approach to inducing non-trivial topological states in complex oxides via artificially designed time-reversal-invariant (001) oxide superlattices. Our design principles are based on a few factors: the band inversion between *d* orbitals of two dissimilar transition metal atoms, a particular parity property of the (001) superlattice geometry, oxygen octahedral rotation pattern, and *d* orbital occupancy. Following the design principles, we use first-principles methods and model Hamiltonian calculations to show concrete examples. We find that a $(SrMO_3)_1/(SrM'O_3)_1$ superlattice is a strong topological insulator (TI) with $M = $ Nb, Ta and $M' = $ Rh, Ir. The most promising candidate is the $(SrTaO_3)_1/(SrIrO_3)_1$ superlattice with the largest atomic spin–orbit coupling and a direct gap of ~20 meV. The topological property is robust against epitaxial strain and weak structural distortions. More interestingly, we show that a $(SrMoO_3)_1/(SrIrO_3)_1$ superlattice has multiple coexisting topological states, including topological insulator (TI) and topological Dirac semi-metal (TDS). Between its highest valence band and its lowest conduction band, there exists a pair of Dirac points (DP) close to the Fermi level as well as Dirac node lines (DNL) that cross the Fermi level. The DP are stabilized by the combination of time-reversal, inversion and C_4 rotation symmetries. They are of type-II (i.e. a tilted Dirac cone) and have a mirror Chern number of 2 (i.e. two Fermi arcs for each DP). The number of DP can be controlled via epitaxial strain. The DNL are protected by non-symmorphic space group ($\mathcal{SG}$) and thus are robust against epitaxial strain. Between the highest valence band and the second highest valence band, as well as between the lowest conduction band and the second lowest conduction

---

[1]Key Laboratory of Polar Materials and Devices, Ministry of Education, East China Normal University, 200241 Shanghai, China. [2]NYU-ECNU Institute of Physics, NYU Shanghai, 200122 Shanghai, China. [3]Department of Electronic Science, East China Normal University, 200241 Shanghai, China. [4]School of Physical Science and Technology, ShanghaiTech University, 201210 Shanghai, China. [5]ShanghaiTech Laboratory for Topological Physics, ShanghaiTech University, 201210 Shanghai, China. [6]Department of Physics, New York University, New York, NY 10012, USA. [7]These authors contributed equally: Zhiwei Liu, Hongquan Liu. ✉email: ligang@shanghaitech.edu.cn; hanghui.chen@nyu.edu

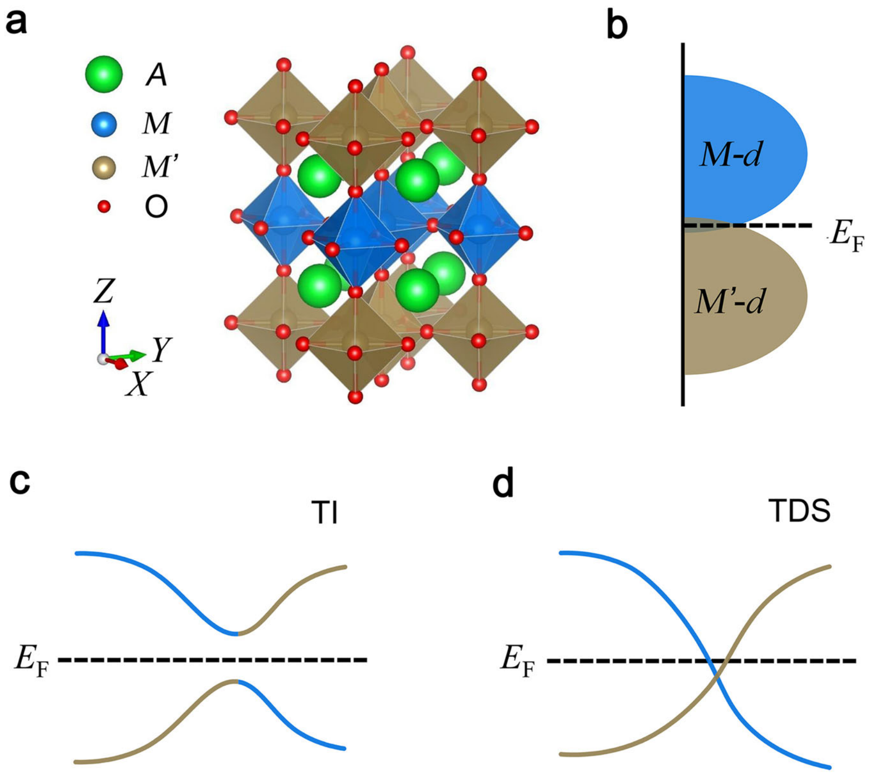

Fig. 1 Crystal structure and schematic electronic structure of (001) oxide superlattices. **a** The crystal structure of a (001) $(AMO_3)_1/(AM'O_3)_1$ superlattice. The green, blue, brown, and red balls represent *A*, *M*, *M*′, and O atoms, respectively. **b** A schematic diagram of density of states of the superlattice. The blue part is the *M-d* states and the brown part is the *M*′*-d* states and the black dash line is the Fermi level. **c, d** A schematic band structure close to the Fermi level where a *M-d* band and a *M*′*-d* band invert. The black dash line is the Fermi level. **c** Spin-orbit coupling opens a full gap between the highest valence band and the lowest conduction band, and non-trivial topological property such as strong topological insulator (TI) may emerge. **d** A *M-d* band and a *M*′*-d* band forms a linear crossing around the Fermi level in the presence of spin-orbit coupling, which may lead to a topological Dirac semi-metal (TDS).

band, a topologically non-trivial gap is opened with a Z_2 index (1;001). The origin of this TI gap is the same as that of the $(SrTaO_3)_1/(SrIrO_3)_1$ superlattice. As a consequence of these multiple topological states coexisting in the $(SrMoO_3)_1/(SrIrO_3)_1$ superlattice, its surface TDS Dirac cone is sandwiched by another two surface TI Dirac cones in the energy-momentum space. The TDS Dirac cone and TI Dirac cones are close to the Fermi level, implying that one can induce a TI-TDS-TI topological state transition via chemical doping or electric-field gating.

Our work demonstrates that artificially designed heterostructures may exhibit emergent topological properties that are absent in their bulk constituents. Therefore in addition to naturally occurring topological materials[56–58], heterostructuring (based on some design principles) provides a different route to emerging topological phenomena.

RESULTS

Design principles

Our basic idea is to construct an artificial band inversion via an oxide superlattice. However, different from *s-p* band inversion or *d-d* band inversion from the same transition metal atom in the previous works[33,34,45,46,59,60], we study *d-d* band inversion between two different transition metal atoms in a (001) oxide superlattice. Panel **a** of Fig. 1 shows the crystal structure of a (001) $(AMO_3)_1/(AM'O_3)_1$ superlattice where *M* and *M*′ are transition metal atoms and *A* is either an alkaline-earth metal or rare-earth metal atom. The oxygen octahedra MO_6 are corner-shared and they alternate along the *z* axis. Panel **b** shows a schematic density of states of the superlattice. We choose *M* to be an early transition metal atom and *M*′ to be a late transition metal atom. Due to electronegativity difference, the *d* orbitals of *M* have higher energies than the *d* orbitals of *M*′[61,62]. Given a proper combination of *M* and *M*′ and their *d* occupancy, *M*–*d* bands and *M*′–*d* bands may overlap with each other around the Fermi level. When spin–orbit coupling (SOC) is included, we can have two situations in which non-trivial topology may emerge. If SOC can open a full gap between the highest valence band and the lowest conduction band, a topological insulating state may emerge, given a proper interaction between *M-d* and *M*′*-d* states (see a schematic band structure in panel **c**)[29,63]. In this case, the (001) superlattice geometry leads to a particular parity property of the two transition metal *d* orbitals, which serves as a key to understand how non-trivial topology arises (see the next section for details). If a linear crossing is stabilized between a *M*–*d* band and a *M*′–*d* band around the Fermi level even in the presence of SOC (see a schematic band structure in panel **d**), then it is possible to get a topological semi-metallic state.

Next we discuss considerations on materials and crystal symmetries. First we choose $A = \mathrm{Sr}$ because the formal valence of Sr is 2+. Due to charge balance, the formal valence of *M* and *M*′ is 4+. That leads to non-polar terminations $[\mathrm{Sr}^{2+}\mathrm{O}^{2-}]$ and $[M^{4+}(\mathrm{O}^{2-})_2]$, which are easier to control than polar terminations in thin film growth[54]. While the above design principles can be extended to magnetic systems, in the current study we focus on time-reversal-invariant systems. Therefore for *M* and *M*′, we study second-row and third-row transition metal atoms, which are more itinerant and less correlated than first-row transition metal atoms[45]. For early transition metal atoms such as Nb and Ta, $SrMO_3$ crystallizes in a cubic structure with no oxygen octahedral (OO) rotation ($\mathcal{SG}$ No. 221 $Pm\bar{3}m$, Glazer notation $a^0a^0a^0$), while for

Table 1. Crystal structure parameters of candidate materials, relevant substrates and proposed oxide superlattices in this work, including crystallographic space group ($\mathcal{SG}$), experimental lattice constants (EXP), and DFT-calculated lattice constants (DFT).

Material	$\mathcal{SG}$	EXP (Å)	DFT (Å)
$SrTiO_3$	$Pm\bar{3}m$ (No. 221)	$a = b = c = 3.903$[113]	$a = b = c = 3.903$
$KTaO_3$	$Pm\bar{3}m$ (No. 221)	$a = b = c = 3.983$[114]	$a = b = c = 3.995$
$SrTaO_3$	$Pm\bar{3}m$ (No. 221)	NA	$a = b = c = 4.029$
$SrMoO_3$	$Pm\bar{3}m$ (No. 221)	$a = b = c = 3.976$[73]	$a = b = c = 3.957$
$SrIrO_3$	$Pnma$ (No. 62)	$a = 5.571, b = 5.601, c = 7.896$[115]	$a = 5.630, b = 5.538, c = 7.863$
$(SrTaO_3)_1/(SrIrO_3)_1$ on $SrTiO_3$	$P4/mbm$ (No. 127)	NA	$a = b = 5.520, c = 8.048$
$(SrMoO_3)_1/(SrIrO_3)_1$ on $KTaO_3$	$P4/mbm$ (No. 127)	NA	$a = b = 5.650, c = 7.780$

late transition metal atoms such as Rh and Ir, $SrMO_3$ crystallizes in an orthorhombic structure with both in-plane and out-of-plane OO rotations ($\mathcal{SG}$ No. 62 $Pnma$, Glazer notation $a^-b^-c^+$). Combining a cubic $Pm\bar{3}m$ perovskite oxide with an orthorhombic $Pnma$ perovskite oxide in a (001) oxide superlattice usually leads to a tetragonal crystal structure ($\mathcal{SG}$ No. 127 $P4/mbm$, Glazer notation $a^0a^0c^-$), which is characterized by an out-of-phase in-plane OO rotation about the stacking direction[53,64]. This crystal structure is 'compromising' in that the in-plane OO rotations are 'forced' into the cubic structure of one perovskite oxide, while the out-of-plane OO rotations are suppressed in the orthorhombic structure of the other perovskite oxide, resulting in only an out-of-phase in-plane OO rotation throughout the superlattice. The out-of-phase in-plane OO rotation in an oxide superlattice leads to cell doubling, a C_4 rotation symmetry and a non-symmorphic $\mathcal{SG}$ ($\mathcal{SG}$ No. 127 $P4/mbm$), which are crucial for Dirac points (DP) and Dirac node lines (DNL).

Finally we discuss d occupancy of M^{4+} and M'^{4+} ions. We consider two cases: $d^1 + d^5$ and $d^2 + d^5$. Due to the cell doubling that is needed to accommodate the OO rotation, the total d occupancy of the $d^1 + d^5$ case is $(1 + 5) \times 2 = 12$, which can be divided by 4, implying a possible insulating ground state (see Supplementary Notes 1 for symmetry analysis). On the other hand, the total d occupancy of the $d^2 + d^5$ case is $(2 + 5) \times 2 = 14$, which is $3 \times 4 + 2$. Given the same symmetry considerations, we must have a gapless system with one band half-filled when the total d occupancy is 14.

Based on the above analysis, we use both first-principles calculations and tight-binding Hamiltonian to demonstrate that the $(SrTaO_3)_1/(SrIrO_3)_1$ superlattice is a strong topological insulator, while the $(SrMoO_3)_1/(SrIrO_3)_1$ superlattice has non-trivial topological gaps, Dirac points and Dirac node lines coexisting in its electronic structure, which lead to multiple surface Dirac cones around the Fermi level. Table 1 summarizes the candidate materials, relevant substrates and proposed oxide superlattices in this study.

Strong TI state in the $(SrTaO_3)_1/(SrIrO_3)_1$ superlattice

We first discuss the $d^1 + d^5$ case and study the (001) $(SrTaO_3)_1/(SrIrO_3)_1$ superlattice grown on a $SrTiO_3$ substrate as a prototype. Both $SrTaO_3$ and $SrIrO_3$ are non-magnetic metals in bulk. Bulk $SrTaO_3$ has a cubic structure ($\mathcal{SG}$ $Pm\bar{3}m$ No. 221), while bulk $SrIrO_3$ crystallizes either in a monoclinic structure of distorted 6*H*-type hexagonal perovskite ($\mathcal{SG}$ $C2/c$ No. 15)[65] or an orthorhombic structure ($\mathcal{SG}$ $Pnma$ No. 62)[66,67]. In thin films, the orthorhombic structure is more favored in $SrIrO_3$[66–68]. After atomic relaxation, our calculations find that the $(SrTaO_3)_1/(SrIrO_3)_1$ superlattice is stabilized in the aforementioned $P4/mbm$ $\mathcal{SG}$ crystal structure, which is characterized by an out-of-phase OO rotation. Ta^{4+} has a nominal d^1 occupancy and Ir^{4+} has a nominal d^5 occupancy. Panel **a** of Fig. 2 shows the density of states (DOS) of the superlattice. The shades and the solid curves correspond to the densities of states calculated using DFT and DFT+SOC, respectively. The gray, red and green shades/curves are total, Ta-d projected and Ir-d projected densities of states, respectively. Due to electronegativity difference, Ta-d states have higher energy than Ir-d states, but they have overlap around the Fermi level. Panel **b** shows the DFT band structure of the $(SrTaO_3)_1/(SrIrO_3)_1$ superlattice close to the Fermi level without SOC. The red curves are Ta-d projected bands and the green curves are Ir-d projected bands. Clearly there are band inversions between Ta-d bands and Ir-d bands. Without SOC the highest valence band and the lowest conduction band form a node surface in the Brillouin zone. Panel **c** shows the DFT+SOC band structure of the superlattice close to the Fermi level. With SOC, a full gap is opened between the highest valence band and the lowest conduction band in the entire Brillouin zone. Because the crystal structure of the $(SrTaO_3)_1/(SrIrO_3)_1$ superlattice has inversion symmetry, we can use the parity rule to easily calculate the Z_2 topological index[25]. Panel **d** shows $\frac{1}{8}$ of the Brillouin zone with the eight time-reversal invariant momentum (TRIM) points explicitly labeled. The parity of each TRIM point is shown in the figure. We find that all the TRIM points have even parity except that Z point has odd parity. Therefore the Z_2 index of the superlattice is (1;001), which is a strong topological insulator. Panel **d** also shows the (100)-projected and (001)-projected surface Brillouin zones. Using the Green function method[69,70], we calculate the (100) surface bands and (001) surface bands in panels **e** and **f**, respectively. In both cases, the topologically protected surface bands traverse the band gap. For the (100) surface, the crossing of the surface bands at $\bar{Z}$ point occurs in the gap and close to the Fermi level (see panel **e**). However, for the (001) surface, the crossing of the surface bands at $\bar{\Gamma}$ point is well below the Fermi level.

To understand why non-trivial topology emerges in the band structure of the $(SrTaO_3)_1/(SrIrO_3)_1$ superlattice, we construct a tight-binding model with the aid of maximally localized Wannier functions. We focus on Ta and Ir atoms, because there are only Ta-d and Ir-d bands around the Fermi level. Ta atoms and Ir atoms are on a respective two-dimensional square lattice, which alternates with each other along the z axis (see panel **a** of Fig. 3). Using the current (xyz) coordinate system in panel **a**, we consider Ta-d_{xz}, d_{yz}, $d_{x^2-y^2}$ orbitals and all five Ir-d orbitals (altogether $(3 + 5) \times 2 = 16$ atomic orbitals). The tight-binding Hamiltonian $H_\lambda(\mathbf{k})$ is:

$$H_\lambda(\mathbf{k}) = H_0(\mathbf{k}) \otimes I_2 + H_{SOC} \tag{1}$$

where $H_0(\mathbf{k})$ is a 16×16 matrix which fits the DFT band structure without SOC, I_2 is a 2×2 identity matrix which is in the spin basis and H_{SOC} is a 32×32 matrix that describes the atomic spin–orbit interaction. $H_0(\mathbf{k})$ can be obtained via maximally localized Wannier

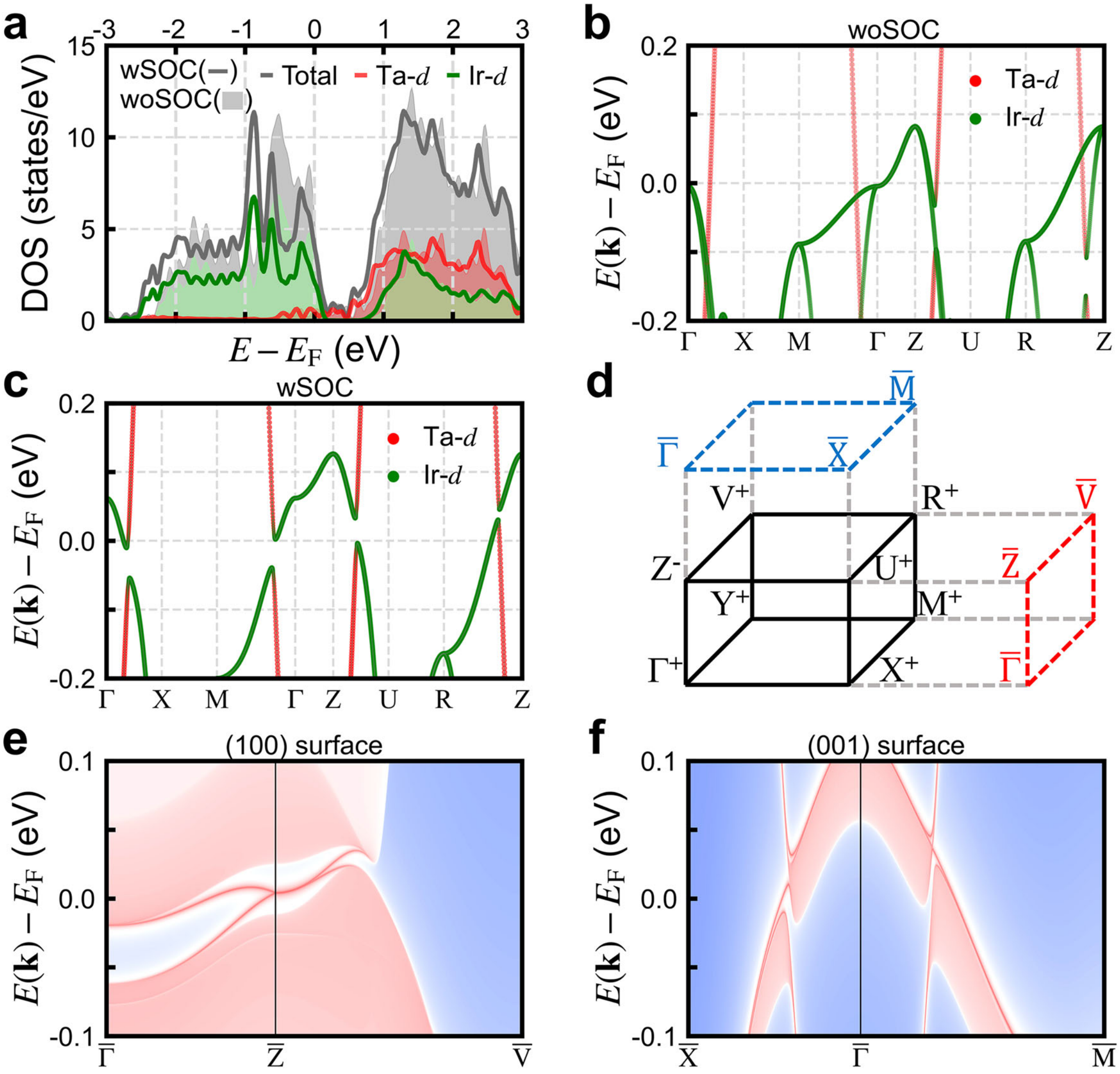

Fig. 2 **Electronic and topological properties of the $(SrTaO_3)_1/(SrIrO_3)_1$ superlattice from first-principles calculations.** **a** Density of states (DOS) of the $(SrTaO_3)_1/(SrIrO_3)_1$ superlattice. The solid curves are the DOS with spin-orbit coupling (SOC) included. The shades are the DOS without SOC. The gray, red, and green curves/shades are total, Ta-*d* projected and Ir-*d* projected DOS. **b** Near Fermi level DFT band structure of the superlattice without SOC. The red and green symbols highlight the atomic projections onto Ta-*d* and Ir-*d* orbitals, respectively. The Fermi level is shifted to the zero energy. **c** Near Fermi level DFT+SOC band structure of the superlattice. The red and green symbols have the same meaning as in panel b. A full gap is opened along the high-symmetry **k**-path. **d** $\frac{1}{8}$ Brillouin zone of the $(SrTaO_3)_1/(SrIrO_3)_1$ superlattice. The eight TRIM points and their parities are explicitly shown. The red and blue dashed lines are $\frac{1}{4}$ surface Brillouin zone which is obtained by projecting the bulk Brillouin zone onto (100) and (001) surfaces. **e** Band structure of (100) semi-infinite slab of the $(SrTaO_3)_1/(SrIrO_3)_1$ superlattice, calculated by the Green-function method. The surface Brillouin zone is highlighted by the red dashed lines in panel d. **f** Band structure of (001) semi-infinite slab of the $(SrTaO_3)_1/(SrIrO_3)_1$ superlattice, calculated by the Green function method. The surface Brillouin zone is highlighted by the blue dashed lines in panel d.

function[71] (see Supplementary Notes 4). $H_{SOC} = \lambda \mathbf{L} \cdot \mathbf{S}$ where λ is the atomic spin-orbit coupling constant (the explicit form of H_{SOC} is shown in Supplementary Notes 6). For simplicity, we assume a common spin–orbit coupling constant λ, since Ta and Ir have close atomic numbers (73 versus 77). The advantage of this simple tight-binding model is that SOC is not absorbed in the basis and thus we can study the SOC effect explicitly. Panel **b** shows the band structure of $H_\lambda(\mathbf{k})$ with $\lambda = 0$ (i.e. no SOC included). We find that with the aid of maximal localized Wannier function, $H_0(\mathbf{k})$ almost exactly reproduces the DFT band structure without SOC. The band inversion between Ta-*d* (red symbols) and Ir-*d* (green symbols) states is clearly seen. Panel **c** shows the band structure of the full Hamiltonian $H_\lambda(\mathbf{k})$ with $\lambda = 0.4$ eV. We find that with SOC included, a full gap is opened between the highest valence band and the lowest conduction band around the Fermi level, which is very similar to the DFT+SOC result (see Fig. 2c). Once the gap is opened with a positive λ, we can calculate the parity of all the valence bands at TRIM points. It turns out that they are identical to those from the DFT+SOC calculations, i.e. a strong topological insulator. In addition, we calculate the minimum direct gap Δ in the Brillouin zone as a function of λ. As panel **d** shows, Δ monotonically increases with λ (up to 0.5 eV). Based on the model Hamiltonian $H_\lambda(\mathbf{k})$, we can calculate the surface bands using the Green function method. Panels **e** and **f** show the (100) and (001) surface bands, respectively. The blue and red dots highlight the projections onto the top surface (TS) and the bottom surface (BS). The surface bands from the model calculations are also very similar to the first-principles calculations. After verifying that the

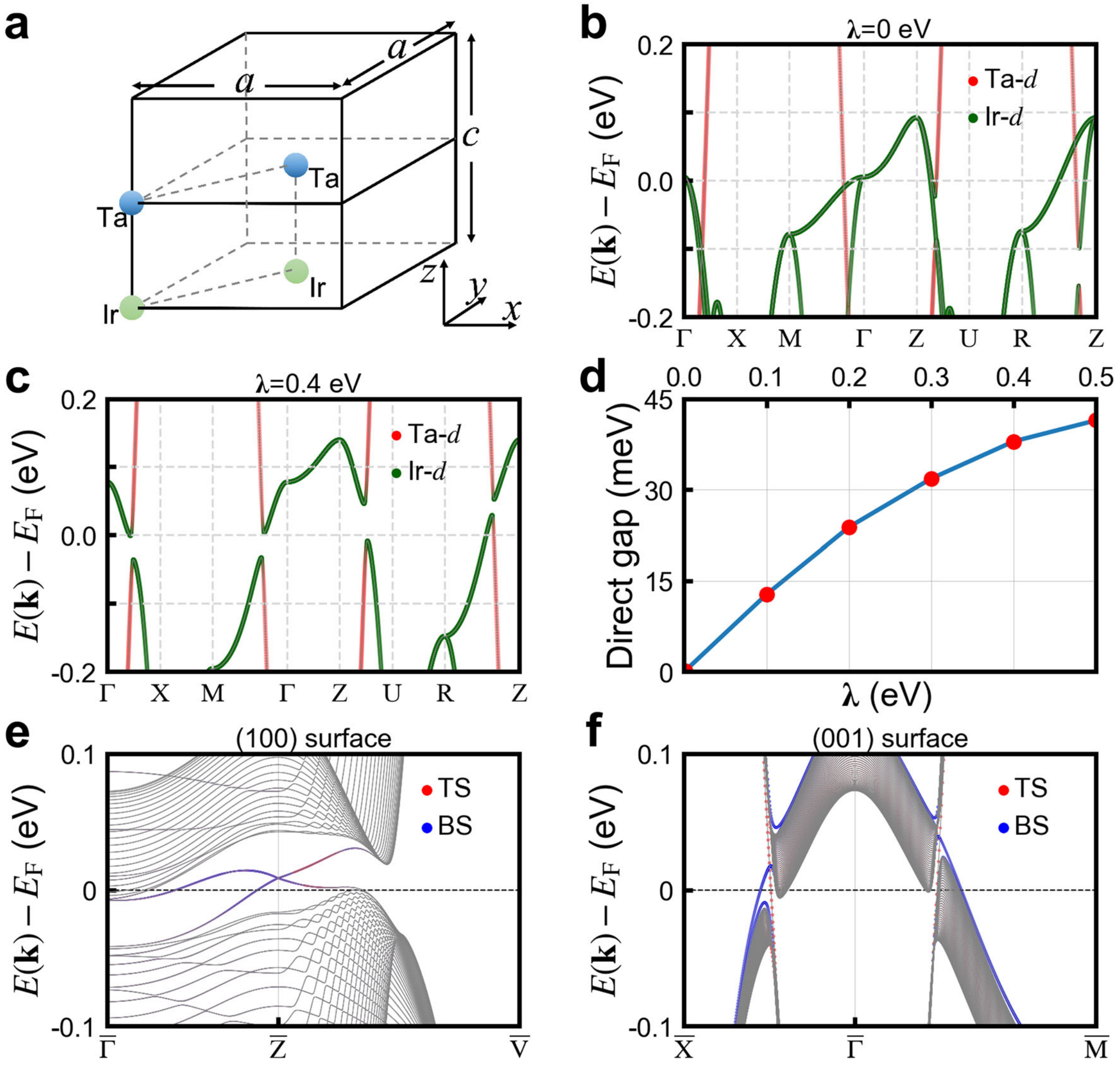

Fig. 3 Electronic and topological properties of the $(SrTaO_3)_1/(SrIrO_3)_1$ superlattice from model calculations. a The lattice sites for Ta and Ir atoms on which a simple tight-binding Hamiltonian model $H_\lambda(\mathbf{k})$ is built. The blue and green balls represent Ta and Ir atoms, respectively. **b** Near-Fermi-level band structure of the tight-binding model $H_\lambda(\mathbf{k})$ with $\lambda = 0$ in the bulk Brillouin zone. The red and green symbols highlight the atomic projection onto Ta-*d* and Ir-*d* orbitals, respectively. The Fermi level is determined by the total occupancy of $N = 12$ and is shifted to the zero energy. Gap is not opened around the Fermi level. **c** Same as panel b except that $\lambda = 0.4$ eV in $H_\lambda(\mathbf{k})$. A gap is opened along the high-symmetry **k**-path. **d** The smallest direct band gap of $H_\lambda(\mathbf{k})$ as a function of λ. The number of valence bands is equal to the total occupancy of $N = 12$. **e** Band structure of (100) semi-infinite slab of the tight-binding model $H_\lambda(\mathbf{k})$ with $\lambda = 0.4$ eV, calculated by using the exact diagonalization method. The red and blue symbols are the projections onto the top surface (TS) and the bottom surface (BS). **f** Same as panel **e** except for (001) semi-infinite slab of the tight-binding model $H_\lambda(\mathbf{k})$ with $\lambda = 0.4$ eV.

simple tight-binding model is adequate to describe the band topology of the $(SrTaO_3)_1/(SrIrO_3)_1$ superlattice, we now elucidate why non-trivial band topology emerges in this system. It depends on several factors. We first count the occupancy: Ta has a d^1 occupancy and Ir has a d^5 occupancy. Therefore in the model the total occupancy is $(1 + 5) \times 2 = 12$. Next we note that all the bands are four-fold degenerate at the TRIM points X, Y, M, U, V, R. This is due to the combination of time-reversal and symmetry operations in $P4/mbm\mathcal{SG}$ (see the symmetry analysis of $P4/mbm\mathcal{SG}$ in Supplementary Notes 1). Considering that the total occupancy is 12, the parity of X, Y, M, U, V, R must be even. Therefore the non-trivial band topology arises from the fact that Γ has even parity and Z has odd parity. However, band inversion occurs at both Γ and Z points. We explain that while both TRIM points have band inversion, the even parity of Γ and the odd parity of Z are closely related to the special coordinates of Ir and Ta in the superlattice. As panel **a** shows, Ir atoms are at $(0, 0, 0)$ and $(\frac{1}{2}, \frac{1}{2}, 0)$ in fractional coordinate system, while Ta atoms are at $(0, 0, \frac{1}{2})$ and $(\frac{1}{2}, \frac{1}{2}, \frac{1}{2})$. The inversion center is at $(0, 0, 0)$, with respect to which inversion operation leads to even number shifts of lattice vectors for Ir atoms, but odd number shifts of lattice vectors for Ta atoms. Consequently, the phase shift induced to the Bloch wavefunction is always 0 for Ir-*d* states at Γ and Z, but for Ta-*d* states the phase shift is 0 at Γ and π at Z. We have band inversion between Ta-*d* and Ir-*d* bands at both Γ and Z points. At Γ, band inversion does not change the parity, which is always even. However, when Ta-*d* band and Ir-*d* band invert at Z, the parity switches and as a result, non-trivial band topology emerges. In summary, the origin of non-trivial topology precisely lies in the special atomic positions of M and M' in the $(AMO_3)_1/(AM'O_3)_1$ superlattice, where the wavefunctions of M and M' atoms gain different phase shift under inversion operation.

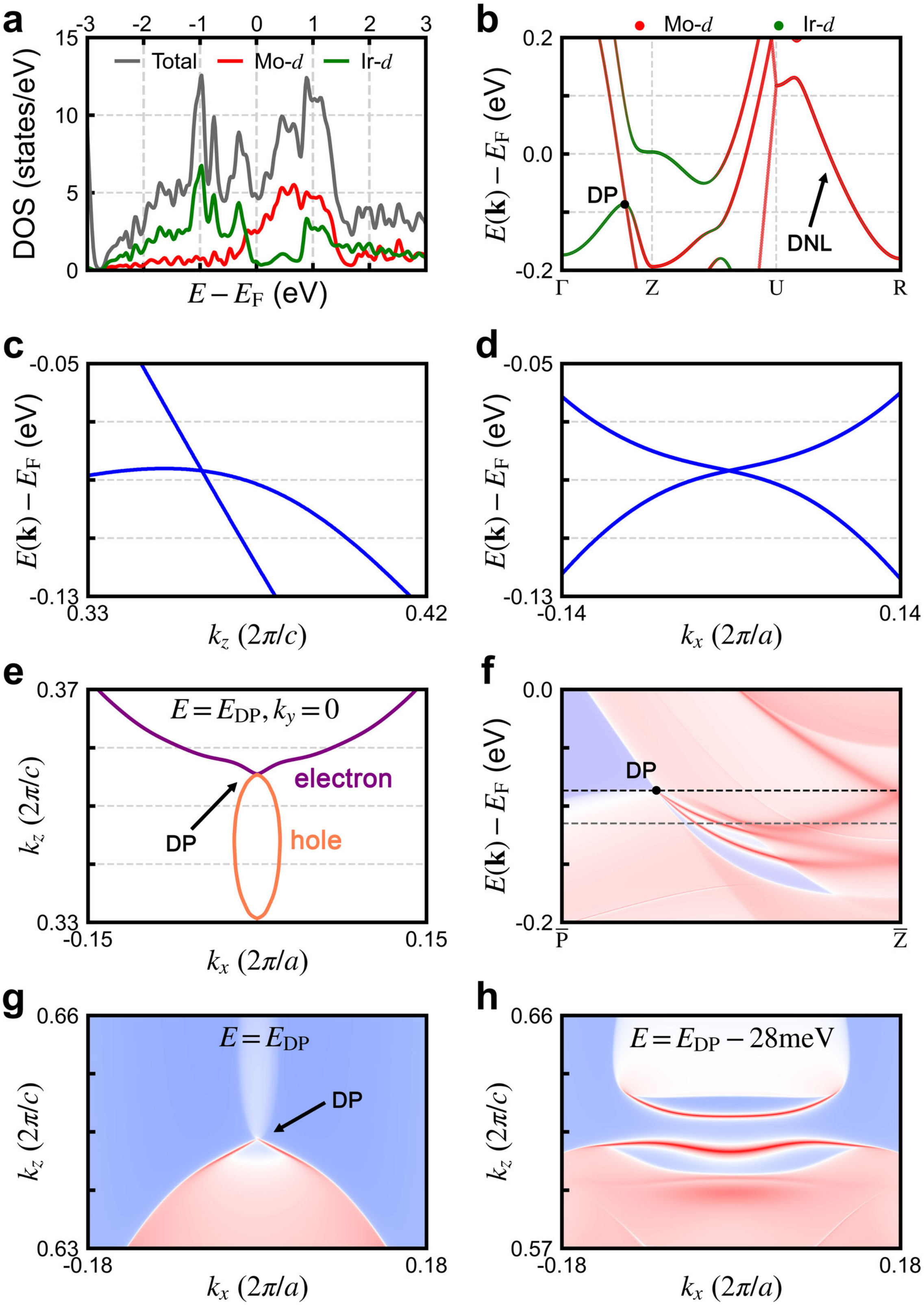

We comment that while we use the inversion symmetry and the parity rule to calculate the Z_2 topological index, we can explicitly show that the strong topological insulating state in the $(SrTaO_3)_1/(SrIrO_3)_1$ superlattice does not depend on the inversion symmetry and/or C_4 rotation symmetry associated with the $P4/mbm\mathcal{SG}$. We can artificially move the Ta or Ir atoms in the superlattice so that the inversion symmetry or C_4 rotation symmetry is explicitly broken. As long as a gap is opened between the highest valence band and the lowest conduction band throughout the Brillouin zone, we can use the Wilson loop

Fig. 4 Electronic and topological properties of the $(SrMoO_3)_1/(SrIrO_3)_1$ superlattice from first-principles calculations. **a** Density of states (DOS) of the $(SrMoO_3)_1/(SrIrO_3)_1$ superlattice, calculated by DFT+SOC method. The gray, red, and green curves are total, Mo-*d* projected and Ir-*d* projected DOS. **b** Near-Fermi-level DFT+SOC band structure of the superlattice. The red and green symbols are Mo-*d* and Ir-*d* projected orbitals, respectively. The black dot highlights a Dirac point (DP) along the $\Gamma \rightarrow Z$ path. The black arrow highlights a Dirac node-line (DNL) along the $U \rightarrow R$ path. **c** Band dispersion in the vicinity of the DP along k_z direction. **d** Band dispersion in the vicinity of the DP along k_x direction. **e** Constant energy at the $k_y = 0$ (k_x, k_z) plane in the bulk Brillouin zone. The constant energy is chosen as the energy of the Dirac point. The purple (orange) curve highlights that it encloses an electron (hole) pocket. The Dirac point emerges where the electron and hole pockets touch each other, which is highlighted by the black arrow. **f** Band structure of (010) semi-infinite slab of the $(SrMoO_3)_1/(SrIrO_3)_1$ superlattice, calculated by using the Green-function method. The **k**-path in the surface Brillouin zone is taken to be $\overline{P} \rightarrow \overline{Z}$, where $\overline{P}$ is (0.0, 0.3) and $\overline{Z}$ is (0.0, 0.5). The black dash line highlights the Dirac point energy. The gray dashed line highlights the energy that is 28 meV below the Dirac point energy. **g** A constant energy contour of band structure of (010) semi-infinite slab of the $(SrMoO_3)_1/(SrIrO_3)_1$ superlattice in the (010) surface Brillouin zone. The constant energy is the energy of DP $E = E_{DP}$, shown by the black line in panel f. **h** The same as panel **g**, except that the constant energy is $E = E_{DP} - 28$ meV, shown by the gray line in panel f.

method[72] to calculate the Z_2 topological index, which still turns out to be (1; 001).

Coexisting TI and TDS states in the $(SrMoO_3)_1/(SrIrO_3)_1$ superlattice

In this section, we study a $d^2 + d^5$ system: the $(SrMoO_3)_1/(SrIrO_3)_1$ superlattice and demonstrate that topological Dirac semi-metal state (TDS) and topological insulator state (TI) coexist in the superlattice. Similar to bulk $SrTaO_3$, $SrMoO_3$ is non-magnetic and crystallizes in a cubic structure ($\mathcal{SG}$ $Pm\bar{3}m$, No. 221)[73]. After atomic relaxation, our calculations find that the $(SrMoO_3)_1/(SrIrO_3)_1$ superlattice also crystallizes in the *P*4/*mbm* structure ($\mathcal{SG}$ No. 127), similar to the $(SrTaO_3)_1/(SrIrO_3)_1$ superlattice. We first consider $KTaO_3$ substrate, which has a very small lattice mismatch with the $(SrMoO_3)_1/(SrIrO_3)_1$ superlattice (the strain effect will be discussed later in this section). Panel **a** of Fig. 4 shows the DFT +SOC density of states of the $(SrMoO_3)_1/(SrIrO_3)_1$ superlattice. Because the electronegativity difference between Mo-*d* and Ir-*d* states is smaller than that between Ta-*d* and Ir-*d* states[62], we can see that Mo-*d* and Ir-*d* states have more overlaps around the Fermi level. Panel **b** of Fig. 4 shows the DFT+SOC band structure around the Fermi level. We find that the highest valence band and the lowest conduction band cross along Γ-Z path. The crossing point is close to the Fermi level (87 meV below the Fermi level). This DP emerges in pairs and only along Γ-Z path $(0,0,k_z)$ and $(0,0,-k_z)$, because of the combination of time-reversal $\mathcal{T}$, inversion $\mathcal{I}$ and C_4 rotation symmetry (associated with $P4/mbm\mathcal{SG}$)[74]. The highest valence band is mainly composed of Ir-*d* orbital and the lowest conduction band is mainly composed of Mo-*d* orbital. The two bands have different eigenvalues of the C_4 rotation operation and thus they cannot hybridize with each other at the crossing point. Therefore the DP is stabilized even in the presence of SOC. However, while the highest valence band and the lowest conduction do not mix along Γ-Z, it is not necessary that the two bands invert. The band inversion in the $(SrMoO_3)_1/(SrIrO_3)_1$ superlattice is a consequence of proper electronegativity difference between Mo and Ir, which can be controlled by external parameters such as epitaxial strain (see discussion below). In addition to the pair of DP, we also find Fermi level crosses a DNL along U-R (see panel **b**). This DNL is protected by the non-symmorphic symmetry associated with $P4/mbm\mathcal{SG}$ (No. 127) together with inversion and time-reversal symmetries. Oxygen octahedral rotations in the crystal structure leads to band folding, which leads to a four-fold degeneracy of all Bloch states along X-M-Y and U-R-V (see symmetry analysis of $P4/mbm\mathcal{SG}$ in Supplementary Notes 1). The Fermi level must cross one of those DNL because of the total occupancy. Mo has a d^2 occupancy and Ir has a d^5 occupancy. Hence the total occupancy is $(2 + 5) \times 2 = 14$, which is $3 \times 4 + 2$ and thus one band must be half-filled. We note that such DNL also exists in the $(SrTaO_3)_1/(SrIrO_3)_1$ superlattice, since the two superlattices have the same symmetries. However, the $(SrTaO_3)_1/(SrIrO_3)_1$ superlattice has a total occupancy of 12, which can be divided by 4. Thus the Fermi level does not cross the DNL of the $(SrTaO_3)_1/(SrIrO_3)_1$ superlattice.

Next we analyze the DP in more details. Panels **c** and **d** of Fig. 4 show the band structure around the DP along k_z and k_x axes. We find that in the vicinity of the DP, the Fermi velocities of the two bands have the same signs along k_z axis, but have opposite signs along k_x axis. This suggests that the DP in the $(SrMoO_3)_1/(SrIrO_3)_1$ superlattice is of type-II[75]. To confirm that, we plot a constant energy contour in the $k_y = 0$ plane (k_x, k_z) in the Brillouin zone with the energy set to be that of the DP (see panel **e**). We find that the DP is a touching point between an electron pocket and a hole pocket, which is the evidence of type-II DP. Furthermore we calculate the topological properties of the DP. We find that the 2D topological invariant $\nu_{2D} = 0$ in both $k_z = 0$ and $k_z = \pi$ planes. However, the mirror Chern number $n_{\mathcal{M}}$ of the $k_z = 0$ plane is equal to 2. These topological properties are distinct from existing TDS Na_3Bi and Cd_3As_2 ($\nu_{2D} = 1$ and $n_{\mathcal{M}} = 1$)[76–79] but identical to VAl_3[75]. The non-trivial $k_z = 0$ mirror Chern number $n_{\mathcal{M}}$ manifests itself as the number of Fermi arc associated with the DP. Panel **f** shows the surface bands along a high-symmetry **k**-path in the (010) surface Brillouin zone. Since the DP is along Γ to Z, when it is projected onto the (010) surface Brillouin zone, the projection is along $\overline{\Gamma}$ to $\overline{Z}$. Panel **f** shows the surface bands of the $(SrMoO_3)_1/(SrIrO_3)_1$ superlattice from $\overline{P}$ (0, 0.3) to $\overline{Z}$. We can clearly see that two Fermi arcs emerge from the projection of the DP at (0, 0.36). They will terminate at the projection of the other DP at (0, −0.36). Panels **g** and **h** show the constant energy contour of the surface bands in the (010) surface Brillouin zone (k_x, k_z). The constant energy value of panel **g** is that of the DP $E = E_{DP}$ (see the black dashed line in panel **f**). The projection of the DP is highlighted by a black arrow. The constant energy value of panel **h** is $E = E_{DP} - 28$ meV (see the gray dashed line in panel **f**). At this energy, the two Fermi arcs are clearly visible in the (010) surface Brillouin zone.

As we mentioned above, the symmetries (time reversal + inversion + C_4 rotation) allow DP to occur, but the actual emergence of DP depends on band inversion. We find that epitaxial strain can control the band inversion and thus the number of DP pairs and their positions in the Brillouin zone. Panels **a**–**c** of Fig. 5 show the DFT+SOC band structure of the $(SrMoO_3)_1/(SrIrO_3)_1$ superlattice under 1%, 2% and 3% compressive strain, respectively. We choose the **k**-path along Γ to Z because DP only appears on that **k**-path. We find that strain can change the relative energy position of the lowest conduction band (blue) and the highest valence band (red) and thus their crossing points close to the Fermi level. When the superlattice is under 1% compressive strain, there is one pair of DP; when it is under 2% compressive strain, there are two pairs of DP; when it is under 3% compressive strain, there are no band crossings and thus no DP. We find that the mirror Chern number of the DP is 2. Panel **d** shows the phase diagram of the $(SrMoO_3)_1/(SrIrO_3)_1$ superlattice as a function of epitaxial strain. From 2% tensile strain to 1.7% compressive strain, the superlattice has one pair of DP. In a narrow compressive strain

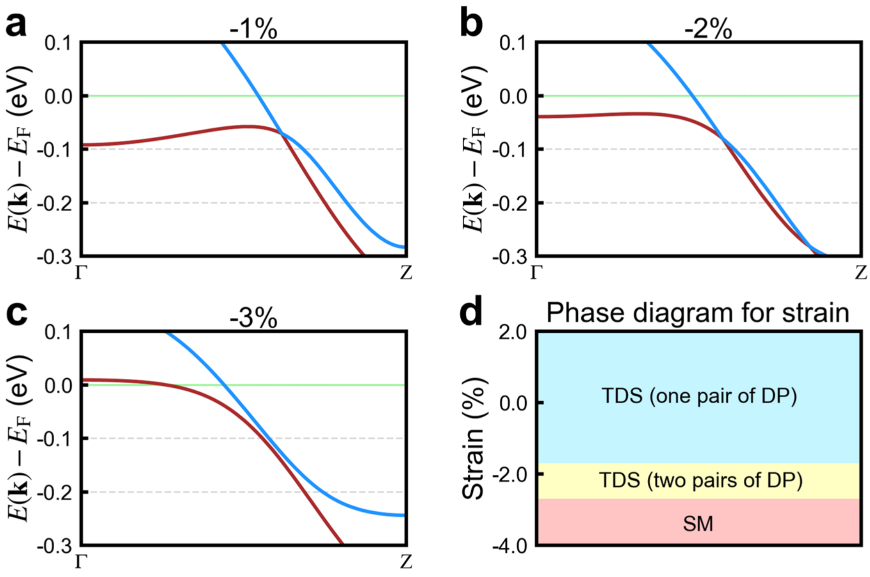

Fig. 5 Strain effects on the Dirac points of the $(\mathrm{SrMoO}_3)_1/(\mathrm{SrIrO}_3)_1$ superlattice. DFT+SOC band structure of the $(\mathrm{SrMoO}_3)_1/(\mathrm{SrIrO}_3)_1$ superlattice along the $\Gamma \to Z$ path under different bi-axial strains. Only the lowest conduction band (blue curve) and the highest valence band (red curve) are shown. The Fermi level is the light green line. **a** 1% compressive strain. **b** 2% compressive strain. **c** 3% compressive strain. **d** Phase diagram of the $(\mathrm{SrMoO}_3)_1/(\mathrm{SrIrO}_3)_1$ superlattice as a function of strain. SM means semi-metals and TDS means topological Dirac semi-metals. When the bi-axial strain is from 2% tensile to 1.7% compressive, the superlattice has one pair of Dirac points (blue area). When the bi-axial strain is from 1.7% compressive to 2.7% compressive, the superlattice has two pairs of Dirac points (yellow area). When the bi-axial strain is from 2.7% to 4% compressive, the superlattice does not have Dirac points.

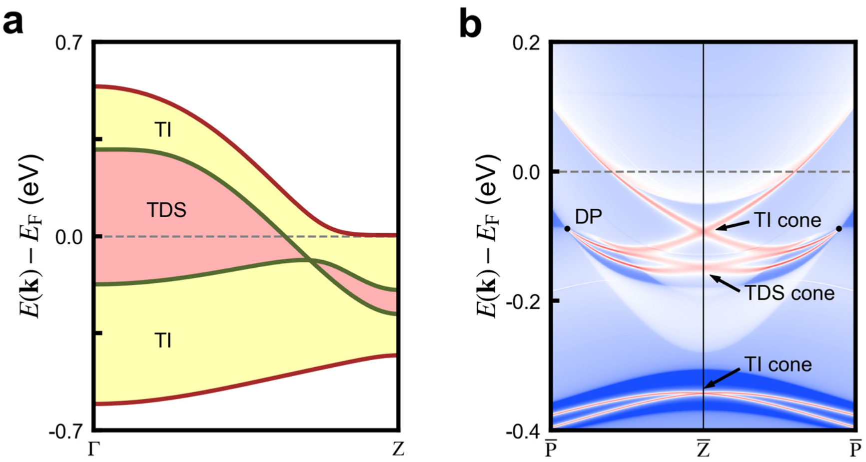

Fig. 6 Coexisting topological Dirac semi-metal and topological insulating states in the $(\mathrm{SrMoO}_3)_1/(\mathrm{SrIrO}_3)_1$ superlattices. a DFT+SOC band structure of $(\mathrm{SrMoO}_3)_1/(\mathrm{SrIrO}_3)_1$ superlattices along $\Gamma \to Z$ path. The two green bands are the highest valence band and the lowest conduction band. They have a linear crossing along Γ to Z with a non-trivial mirror Chern number, which leads to a topological Dirac semi-metals (TDS) state (highlighted by light red). The red bands and green bands do not have crossing in the entire Brillouin zone and the gap between them (highlighted by light yellow) is topologically non-trivial with Z_2 index (1;001). **b** Band structure of (010) semi-infinite slab of the $(\mathrm{SrMoO}_3)_1/(\mathrm{SrIrO}_3)_1$ superlattice, calculated by using the Green-function method. The red indicates the surface states. The **k**-path in the surface Brillouin zone is taken to be $\overline{P} \to \overline{Z}$, where $\overline{P}$ is (0.0, 0.3) and $\overline{Z}$ is (0.0, 0.5). The black dots highlight Dirac point (DP). The black arrows highlight TI surface Dirac cone and TDS surface Dirac cone. The TDS surface Dirac cone is sandwiched between two TI surface Dirac cone in the energy-momentum space.

range (from 1.7% to 2.7%), the superlattice has two pairs of DP. When the compressive strain exceeds 2.7%, the superlattice does not have DP. KTaO_3 has negligible lattice mismatch to the $(\mathrm{SrMoO}_3)_1/(\mathrm{SrIrO}_3)_1$ superlattice and therefore the superlattice on a KTaO_3 substrate has one pair of DP. The more widely used substrate SrTiO_3 imposes a 2.3% compressive strain on the $(\mathrm{SrMoO}_3)_1/(\mathrm{SrIrO}_3)_1$ superlattice and thus the superlattice on a SrTiO_3 substrate has two pairs of DP. However, in all the above cases, DNL still exists and the Fermi level must cross a DNL, which is guaranteed by the non-symmorphic symmetry and the total occupancy. Similar to the previous $(\mathrm{SrTaO}_3)_1/(\mathrm{SrIrO}_3)_1$ superlattice, we can also build a tight-binding Hamiltonian $H(\mathbf{k}) = H_0(\mathbf{k}) \otimes I_2 + H_{\mathrm{SOC}}$ to study the SOC effects on the DP (see Supplementary Notes 7). We find that theoretically, tuning the strength of SOC can also control the band inversion and thus the number of DP pairs. For a range of SOC strength (reasonable for Mo and Ir), the tight-binding model finds one pair of DP along Γ to Z.

Finally, we demonstrate the peculiar topological properties of the $(\mathrm{SrMoO}_3)_1/(\mathrm{SrIrO}_3)_1$ superlattice: the coexistence of TDS and TI. Panel **a** of Fig. 6 shows the near-Fermi-level band structure of the $(\mathrm{SrMoO}_3)_1/(\mathrm{SrIrO}_3)_1$ superlattice. The highest valence band and the lowest conduction band have a linear crossing along Γ to Z with a non-trivial mirror Chern number. This leads to the aforementioned TDS state, which is highlighted by the light red shade in Fig. 6a. However, the highest valence band and the second highest valence band, as well as the lowest conduction band and the second lowest conduction band do not have crossing in the entire Brillouin zone and the gap between them (highlighted by the light yellow shades) turns out to be topologically non-trivial with Z_2 index (1;001). The emergence of those TI states has the same origin as the $(SrTaO_3)_1/(SrIrO_3)_1$ superlattice. Panel **b** shows the (010) projected surface bands of the $(SrMoO_3)_1/(SrIrO_3)_1$ superlattice. The high-symmetry **k**-path is taken from $\overline{P}$ (0, 0.3) to $\overline{Z}$ to $\overline{P}$ in the 2D surface Brillouin zone. The red highlights the projection of the surface bands. We find that the TDS surface Dirac cone is sandwiched between two TI surface Dirac cone in the energy-momentum space. In particular, the upper TI surface Dirac cone crosses the Fermi level. With hole doping, the Fermi level may be shifted so as to cross the TDS surface Dirac cone and the lower TI surface Dirac cone. Such a TI-TDS-TI topological phase transition may be achieved via chemical doping[80] or electric-field gating[81]. The coexistence of a TI surface Dirac cone and a TDS surface Dirac cone near the Fermi level was also found in iron-based superconductors such as FeSe[82]. In those materials, the band inversion is between Fe-$d_{xz/yz}$ orbitals and ligand-p_z orbitals and the non-trivial topology arises because of the dissimilar orbital parity (a different mechanism from the one in this work). Furthermore in our case of the $(SrMoO_3)_1/(SrIrO_3)_1$ superlattice, the topological surface bands are richer in that there are two TI surface Dirac cones, which sandwich a TDS surface Dirac cone.

DISCUSSION

Before we conclude, we make a few comments. First, iridates such as Sr_2IrO_4 and $(SrTiO_3)_1/(SrIrO_3)_1$ superlattice exhibit canted antiferromagnetism (AFM) at low temperatures[83–86]. We investigate whether canted AFM may also emerge in the $(SrTaO_3)_1/(SrIrO_3)_1$ and $(SrMoO_3)_1/(SrIrO_3)_1$ superlattices. From DFT+U+SOC calculations, we find that up to U_{Ir} of 4 eV, no canted AFM is stabilized in either superlattice and thus their topological properties remain robust (see Supplementary Notes 5). In literature, considering that Ir is a third-row transition metal element with more extended 5d orbitals, its effective Hubbard U ranges between 1 and 3 eV[87–89]. Second, it is well known that DFT calculations with semi-local exchange-correlation functionals underestimate the oxygen-p and metal-d separation (p-d separation) in complex oxides. However, in our study, we focus on d-d band inversion. While the p-d separation is underestimated in each SrMO$_3$, the d-d separation is less affected by the semi-local exchange-correlation functionals, as demonstrated in the previous study[90]. Third, both in the $(SrTaO_3)_1/(SrIrO_3)_1$ and $(SrMoO_3)_1/(SrIrO_3)_1$ superlattices, their (100) surface exhibits topologically non-trivial surface states. While the (001) surface is the most natural surface for a (001)-grown oxide superlattice, a (100) or (010) surface can also be obtained by either cleaving the sample or mechanically polishing the sample[91,92]. Such preparation of (100) or (010) surfaces is routinely made in transmission electron microscopy (TEM) and cross-sectional scanning tunneling microscopy (STM) measurements[93–96]. Finally, we comment on how one may separate the topological surface bands from the bulk spectrum. We notice that in both superlattices ($(SrTaO_3)_1/(SrIrO_3)_1$ and $(SrMoO_3)_1/(SrIrO_3)_1$), the topological surface states overlap with the bulk spectrum in the energy window. However, as Figs. 2e and 4f show, in the energy window that is close to the Fermi level, the topological surface bands and the bulk spectrum are separated in the momentum space. This enables direct spectroscopic observation (such as ARPES)[97,98]. In addition, in actual experiments, disorders are inevitable, which may suppress the bulk conduction via the Anderson localization[99]. By contrast, the conduction from the topological surface bands can evade the Anderson localization (as long as the defect is non-magnetic)[18]. This scenario likely occurs to the $(SrTaO_3)_1/(SrIrO_3)_1$ superlattice, whose bulk Fermi surface consists of small electron and hole pockets. Finally, while the bulk topological properties protect the *presence* of the surface states[18], the details of the surface states can also be tuned in experiment. Adsorption and removal of non-magnetic atoms on the surface as well as different surface terminations can modify the curvature of the topological surface bands, which provides another means to separate the surface states from the bulk spectrum[100–104].

In summary, we combine first-principles calculations and tight-binding models to show that between the highest valence band and the lowest conduction band, the $(SrTaO_3)_1/(SrIrO_3)_1$ superlattice exhibits a strong topological insulating state (TI) and the $(SrMoO_3)_1/(SrIrO_3)_1$ superlattice is a topological Dirac semi-metal (TDS) that is characterized by a pair of type-II DP with a mirror Chern number of 2, as well as DNL protected by non-symmorphic space group. The $(SrMoO_3)_1/(SrIrO_3)_1$ superlattice also exhibits a strong topological insulating state between the highest valence band and the second highest valence band, as well as the lowest conduction band and the second lowest conduction band. The coexistence of multiple topological states in the $(SrMoO_3)_1/(SrIrO_3)_1$ superlattice leads to a characteristic 'sandwich' structure of the surface bands: one TDS surface Dirac cone lies between two TI surface Dirac cones in the energy-momentum space. For both TI and TDS states, the non-trivial band topology arises from band inversion between d states of two different transition metal atoms, combined with proper d occupancy and time-reversal symmetry. In the TDS state, crystal symmetry (C_4 rotation symmetry and non-symmorphic $P4/mbm$ space group) also plays a crucial role. The design principle is also applicable to first-row transition metal atoms whose d orbitals are more strongly correlated and may break time-reversal symmetry with long-range magnetic order. In a (001) $(AMO_3)/(AM'O_3)$ oxide superlattice with stronger correlation effects on transition metal d orbitals, other topological states such as quantum anomalous Hall state and Weyl semi-metal state may emerge. This will be in our future research.

METHODS

We perform density functional theory (DFT)[105,106] calculations, as implemented in Vienna Ab Initio Simulation Package (VASP)[107,108]. We use the generalized gradient approximation with the Perdew-Burke-Ernzerhof parameterization revised for solids (PBEsol)[109] as the exchange-correlation functional. We use an energy cutoff of 600 eV and a $10 \times 10 \times 8$ Monkhorst-Pack **k**-mesh to sample the Brillouin zone[110] of the superlattice. Spin–orbit coupling (SOC) is self-consistently included in all the calculations unless otherwise specified. The convergence threshold for the self-consistent calculation is 10^{-6} eV. Atomic relaxation is converged when each force component is smaller than 0.01 eV Å^{-1} and pressure on the simulation cell is <0.5 kbar. For bi-axial strain calculations, we fix the two in-plane lattice constants and allow the out-of-plane lattice constant (along the stacking direction) to fully relax. The strain is defined as $\xi = (a - a_0)/a_0 \times 100\%$ where a_0 is the DFT optimized pseudo-tetragonal lattice constant and a is the theoretical lattice constant of the substrate.

We employ the Wannier90 packages[111] to construct the maximally localized Wannier functions (MLWF)[71]. We use two sets of Wannier functions. The first set of Wannier functions is to fit the band structure with SOC. This set of Wannier functions, combined with Green function method, is used to calculate the surface bands, as implemented in WannierTools[112]. The second set of Wannier functions is to fit the band structure without SOC. This set of Wannier function is used to construct the tight-binding model in which atomic SOC interaction is explicitly shown in an analytical form and studied.

DATA AVAILABILITY

The data that support the findings of this study are available from the corresponding author upon reasonable request.

CODE AVAILABILITY

The electronic structure calculations were performed using the proprietary code VASP[108], the open-source codes Wannier90[111] and WannierTools[112]. Both Wannier90 and WannierTools are freely distributed on academic use under the Massachusetts Institute of Technology (MIT) License.

Received: 3 March 2022; Accepted: 14 September 2022;

REFERENCES

1. Anisimov, V. I., Zaanen, J. & Andersen, O. K. Band theory and Mott insulators: Hubbard *U* instead of stoner *I*. *Phys. Rev. B* **44**, 943–954 (1991).
2. Mott, N. F. The basis of the electron theory of metals, with special reference to the transition metals. *Proc. Phys. Soc. A* **62**, 416–422 (1949).
3. MOTT, N. F. Metal-insulator transition. *Rev. Mod. Phys.* **40**, 677–683 (1968).
4. Imada, M., Fujimori, A. & Tokura, Y. Metal-insulator transitions. *Rev. Mod. Phys.* **70**, 1039–1263 (1998).
5. Zubko, P., Gariglio, S., Gabay, M., Ghosez, P. & Triscone, J.-M. Interface physics in complex oxide heterostructures. *Annu. Rev. Condens. Matter Phys.* **2**, 141–165 (2011).
6. Tokura, Y. & Nagaosa, N. Orbital physics in transition-metal oxides. *Science* **288**, 462–468 (2000).
7. Seidel, J. et al. Conduction at domain walls in oxide multiferroics. *Nat. Mater.* **8**, 229–234 (2009).
8. Chapon, L. C. et al. Structural anomalies and multiferroic behavior in magnetically frustrated $TbMn_2O_5$. *Phys. Rev. Lett.* **93**, 177402 (2004).
9. Kimura, T. et al. Magnetocapacitance effect in multiferroic $BiMnO_3$. *Phys. Rev. B* **67**, 180401 (2003).
10. Spaldin, N. A. & Ramesh, R. Advances in magnetoelectric multiferroics. *Nat. Mater.* **18**, 203–212 (2019).
11. Fiebig, M., Lottermoser, T., Meier, D. & Trassin, M. The evolution of multiferroics. *Nat. Rev. Mater.* **1**, 16046 (2016).
12. Cheong, S.-W. & Mostovoy, M. Multiferroics: a magnetic twist for ferroelectricity. *Nat. Mater.* **6**, 13–20 (2007).
13. Bednorz, J. G. & Müller, K. A. Possible high T_c superconductivity in the Ba-La-Cu-O system. *Z. Phys. B Condens. Matter* **64**, 189–193 (1986).
14. Dagotto, E. Correlated electrons in high-temperature superconductors. *Rev. Mod. Phys.* **66**, 763–840 (1994).
15. Tranquada, J. M., Sternlieb, B. J., Axe, J. D., Nakamura, Y. & Uchida, S. Evidence for stripe correlations of spins and holes in copper oxide superconductors. *Nature* **375**, 561–563 (1995).
16. Keimer, B., Kivelson, S. A., Norman, M. R., Uchida, S. & Zaanen, J. From quantum matter to high-temperature superconductivity in copper oxides. *Nature* **518**, 179–186 (2015).
17. Lee, P. A., Nagaosa, N. & Wen, X.-G. Doping a Mott insulator: physics of high-temperature superconductivity. *Rev. Mod. Phys.* **78**, 17–85 (2006).
18. Hasan, M. Z. & Kane, C. L. Colloquium : topological insulators. *Rev. Mod. Phys.* **82**, 3045–3067 (2010).
19. Qi, X.-L. & Zhang, S.-C. Topological insulators and superconductors. *Rev. Mod. Phys.* **83**, 1057–1110 (2011).
20. Lu, C., Wang, C., Xiao, M., Zhang, Z. & Chan, C. Topological rainbow concentrator based on synthetic dimension. *Phys. Rev. Lett.* **126**, 113902 (2021).
21. Lu, L., Joannopoulos, J. D. & Soljačić, M. Topological photonics. *Nat. Photon.* **8**, 821–829 (2014).
22. Luo, L. et al. Observation of a phononic higher-order Weyl semimetal. *Nat. Mater.* **20**, 794–799 (2021).
23. Ma, G., Xiao, M. & Chan, C. T. Topological phases in acoustic and mechanical systems. *Nat. Rev. Phys.* **1**, 281–294 (2019).
24. Weng, H. et al. Topological node-line semimetal in three-dimensional graphene networks. *Phys. Rev. B* **92**, 045108 (2015).
25. Fu, L., Kane, C. L. & Mele, E. J. Topological insulators in three dimensions. *Phys. Rev. Lett.* **98**, 106803 (2007).
26. Liu, Z. K. et al. Discovery of a three-dimensional topological Dirac semimetal, Na_3Bi. *Science* **343**, 864–867 (2014).
27. Hsieh, D. et al. A topological Dirac insulator in a quantum spin hall phase. *Nature* **452**, 970–974 (2008).
28. König, M. et al. Quantum spin hall insulator state in HgTe quantum wells. *Science* **318**, 766–770 (2007).
29. Bernevig, B. A., Hughes, T. L. & Zhang, S.-C. Quantum spin hall effect and topological phase transition in HgTe quantum wells. *Science* **314**, 1757–1761 (2006).
30. Zhang, H. et al. Topological insulators in Bi_2Se_3, Bi_2Te_3 and Sb_2Te_3 with a single Dirac cone on the surface. *Nat. Phys.* **5**, 438–442 (2009).
31. Xia, Y. et al. Observation of a large-gap topological-insulator class with a single Dirac cone on the surface. *Nat. Phys.* **5**, 398–402 (2009).
32. Zhang, Y. et al. Crossover of the three-dimensional topological insulator Bi_2Se_3 to the two-dimensional limit. *Nat. Phys.* **6**, 584–588 (2010).
33. Jin, H., Rhim, S. H., Im, J. & Freeman, A. J. Topological oxide insulator in cubic perovskite structure. *Sci. Rep.* **3**, 1651 (2013).
34. Yan, B., Jansen, M. & Felser, C. A large-energy-gap oxide topological insulator based on the superconductor $BaBiO_3$. *Nat. Phys.* **9**, 709–711 (2013).
35. Mohanta, N. et al. Semi-Dirac and Weyl fermions in transition metal oxides. *Phys. Rev. B* **104**, 235121 (2021).
36. Carter, J.-M., Shankar, V. V., Zeb, M. A. & Kee, H.-Y. Semimetal and topological insulator in perovskite iridates. *Phys. Rev. B* **85**, 115105 (2012).
37. Chen, Y., Lu, Y.-M. & Kee, H.-Y. Topological crystalline metal in orthorhombic perovskite iridates. *Nat. Commun.* **6**, 6593 (2015).
38. Fujioka, J. et al. Strong-correlation induced high-mobility electrons in Dirac semimetal of perovskite oxide. *Nat. Commun.* **10**, 362 (2019).
39. Yamada, R. et al. Large variation of Dirac semimetal state in perovskite $CaIrO_3$ with pressure-tuning of electron correlation. *Phys. Rev. Lett.* **123**, 216601 (2019).
40. Rüegg, A. & Fiete, G. A. Topological insulators from complex orbital order in transition-metal oxides heterostructures. *Phys. Rev. B* **84**, 201103 (2011).
41. Lado, J. L., Pardo, V. & Baldomir, D. *Abinitio* study of Z_2 topological phases in perovskite (111) $(SrTiO_3)_7/(SrIrO_3)_2$ and $(KTaO_3)_7/(KPtO_3)_2$ multilayers. *Phys. Rev. B* **88**, 155119 (2013).
42. Zhang, H., Huang, H., Haule, K. & Vanderbilt, D. Quantum anomalous hall phase in (001) double-perovskite monolayers via intersite spin-orbit coupling. *Phys. Rev. B* **90**, 165143 (2014).
43. Hwang, H. Y. et al. Emergent phenomena at oxide interfaces. *Nat. Mater.* **11**, 103–113 (2012).
44. Ahn, C. et al. Designing and controlling the properties of transition metal oxide quantum materials. *Nat. Mater.* **20**, 1462–1468 (2021).
45. Xiao, D., Zhu, W., Ran, Y., Nagaosa, N. & Okamoto, S. Interface engineering of quantum hall effects in digital transition metal oxide heterostructures. *Nat. Commun.* **2**, 596 (2011).
46. Chakhalian, J., Liu, X. & Fiete, G. A. Strongly correlated and topological states in [111] grown transition metal oxide thin films and heterostructures. *APL Mater.* **8**, 050904 (2020).
47. Kane, C. L. & Mele, E. J. Z_2 topological order and the quantum spin hall effect. *Phys. Rev. Lett.* **95**, 146802 (2005).
48. Kane, C. L. & Mele, E. J. Quantum spin hall effect in graphene. *Phys. Rev. Lett.* **95**, 226801 (2005).
49. Shitade, A. et al. Quantum spin hall effect in a transition metal oxide Na_2IrO_3. *Phys. Rev. Lett.* **102**, 256403 (2009).
50. Halperin, B. I., Lee, P. A. & Read, N. Theory of the half-filled Landau level. *Phys. Rev. B* **47**, 7312–7343 (1993).
51. Pan, L. et al. Observation of quantum anomalous hall effect and exchange interaction in topological insulator/antiferromagnet heterostructure. *Adv. Mater.* **32**, 2001460 (2020).
52. Haldane, F. D. M. Model for a quantum hall effect without Landau levels: Condensed-matter realization of the "parity anomaly". *Phys. Rev. Lett.* **61**, 2015–2018 (1988).
53. Cui, Z. et al. Correlation-driven eightfold magnetic anisotropy in a two-dimensional oxide monolayer. *Sci. Adv.* **6**, eaay0114 (2020).
54. Schlom, D. G., Chen, L.-Q., Pan, X., Schmehl, A. & Zurbuchen, M. A. A thin film approach to engineering functionality into oxides. *J. Am. Ceram. Soc.* **91**, 2429–2454 (2008).
55. Ramesh, R. & Schlom, D. G. Creating emergent phenomena in oxide superlattices. *Nat. Rev. Mater.* **4**, 257–268 (2019).
56. Tang, F., Po, H. C., Vishwanath, A. & Wan, X. Comprehensive search for topological materials using symmetry indicators. *Nature* **566**, 486–489 (2019).
57. Zhang, T. et al. Catalogue of topological electronic materials. *Nature* **566**, 475–479 (2019).
58. Vergniory, M. G. et al. A complete catalogue of high-quality topological materials. *Nature* **566**, 480–485 (2019).
59. Young, S. M. et al. Dirac semimetal in three dimensions. *Phys. Rev. Lett.* **108**, 140405 (2012).
60. Steinberg, J. A. et al. Bulk Dirac points in distorted spinels. *Phys. Rev. Lett.* **112**, 036403 (2014).

61. Chen, H., Millis, A. J. & Marianetti, C. A. Engineering correlation effects via artificially designed oxide superlattices. *Phys. Rev. Lett.* **111**, 116403 (2013).
62. Chen, H. & Millis, A. Charge transfer driven emergent phenomena in oxide heterostructures. *J. Phys. Condens. Matter* **29**, 243001 (2017).
63. Weng, H., Dai, X. & Fang, Z. Exploration and prediction of topological electronic materials based on first-principles calculations. *MRS Bull.* **39**, 849–858 (2014).
64. Verissimo-Alves, M., García-Fernández, P., Bilc, D. I., Ghosez, P. & Junquera, J. Highly confined spin-polarized two-dimensional electron gas in $SrTiO_3/SrRuO_3$ superlattices. *Phys. Rev. Lett.* **108**, 107003 (2012).
65. Hsu, Y.-T. et al. Evidence for strong electron correlations in a nonsymmorphic Dirac semimetal. *npj Quant. Mater.* **6**, 92 (2021).
66. Wu, F.-X. et al. Metal-insulator transition in $SrIrO_3$ with strong spin-orbit interaction. *J. Phys. Condens. Matter* **25**, 125604 (2013).
67. Biswas, A., Kim, K.-S. & Jeong, Y. H. Metal insulator transitions in perovskite $SrIrO_3$ thin films. *J. Appl. Phys.* **116**, 213704 (2014).
68. Nie, Y. et al. Interplay of spin-orbit interactions, dimensionality, and octahedral rotations in semimetallic $SrIrO_3$. *Phys. Rev. Lett.* **114**, 016401 (2015).
69. Lopez Sancho, M. P., Lopez Sancho, J. M. & Rubio, J. Quick iterative scheme for the calculation of transfer matrices: application to Mo (100). *J. Phys. F: Met. Phys.* **14**, 1205 (1984).
70. Lopez Sancho, M. P., Lopez Sancho, J. M., Sancho, J. M. L. & Rubio, J. Highly convergent schemes for the calculation of bulk and surface Green functions. *J. Phys. F: Met. Phys.* **15**, 851 (1985).
71. Marzari, N., Mostofi, A. A., Yates, J. R., Souza, I. & Vanderbilt, D. Maximally localized Wannier functions: Theory and applications. *Rev. Mod. Phys.* **84**, 1419–1475 (2012).
72. Yu, R., Qi, X. L., Bernevig, A., Fang, Z. & Dai, X. Equivalent expression of Z_2 topological invariant for band insulators using the non-Abelian Berry connection. *Phys. Rev. B* **84**, 075119 (2011).
73. Macquart, R. B., Kennedy, B. J. & Avdeev, M. Neutron diffraction study of phase transitions in perovskite-type strontium molybdate $SrMoO_3$. *J. Solid State Chem.* **183**, 250–255 (2010).
74. Yang, B.-J. & Nagaosa, N. Classification of stable three-dimensional Dirac semimetals with nontrivial topology. *Nat. Commun.* **5**, 4898 (2014).
75. Chang, T.-R. et al. Type-II symmetry-protected topological Dirac semimetals. *Phys. Rev. Lett.* **119**, 026404 (2017).
76. Wang, Z. et al. Dirac semimetal and topological phase transitions in A_3Bi ($A =$ Na, K, Rb). *Phys. Rev. B* **85**, 195320 (2012).
77. Neupane, M. et al. Observation of a three-dimensional topological Dirac semimetal phase in high-mobility Cd_3As_2. *Nat. Commun.* **5**, 3786 (2014).
78. Borisenko, S. et al. Experimental realization of a three-dimensional Dirac semimetal. *Phys. Rev. Lett.* **113**, 027603 (2014).
79. Wang, Z., Weng, H., Wu, Q., Dai, X. & Fang, Z. Three-dimensional Dirac semimetal and quantum transport in Cd_3As_2. *Phys. Rev. B* **88**, 125427 (2013).
80. Joucken, F. et al. Charge transfer and electronic doping in nitrogen-doped graphene. *Sci. Rep.* **5**, 14564 (2015).
81. Wang, Z. et al. The ambipolar transport behavior of WSe_2 transistors and its analogue circuits. *NPG Asia Mater.* **10**, 703–712 (2018).
82. Zhang, P. et al. Multiple topological states in iron-based superconductors. *Nat. Phys.* **15**, 41–47 (2019).
83. Crawford, M. K. et al. Structural and magnetic studies of Sr_2IrO_4. *Phys. Rev. B* **49**, 9198–9201 (1994).
84. Fujiyama, S. et al. Two-dimensional heisenberg behavior of $J_{\mathrm{eff}} = 1/2$ isospins in the paramagnetic state of the spin-orbital Mott insulator Sr_2IrO_4. *Phys. Rev. Lett.* **108**, 247212 (2012).
85. Kim, B. J. et al. Novel $J_{\mathrm{eff}} = 1/2$ Mott state induced by relativistic spin-orbit coupling in Sr_2IrO_4. *Phys. Rev. Lett.* **101**, 076402 (2008).
86. Matsuno, J. et al. Engineering a spin-orbital magnetic insulator by tailoring superlattices. *Phys. Rev. Lett.* **114**, 247209 (2015).
87. Bhowal, S. & Satpathy, S. Electronic structure and anomalous hall effect in the ferromagnetic $3d-5d$ superlattice $SrMnO_3/SrIrO_3$. *Phys. Rev. B* **99**, 245145 (2019).
88. Liu, X. et al. Interfacial charge-transfer Mott state in iridate-nickelate superlattices. *Proc. Natl Acad. Sci. USA* **116**, 19863–19868 (2019).
89. Liu, P. et al. Anisotropic magnetic couplings and structure-driven canted to collinear transitions in Sr_2IrO_4 by magnetically constrained noncollinear DFT. *Phys. Rev. B* **92**, 054428 (2015).
90. Chen, H., Park, H., Millis, A. J. & Marianetti, C. A. Charge transfer across transition-metal oxide interfaces: Emergent conductance and electronic structure. *Phys. Rev. B* **90**, 245138 (2014).
91. Shibata, N. et al. Direct imaging of reconstructed atoms on TiO_2 (110) surfaces. *Science* **322**, 570–573 (2008).
92. Liu, L., Sun, Y., Cheng, Z., Zhu, J. & Yu, R. Subsurface reconstruction and saturation of surface bonds. *Sci. Bull.* **63**, 1570–1575 (2018).
93. Yu, T. et al. Polarity and spin-orbit coupling induced strong interfacial exchange coupling: An asymmetric charge transfer in iridate-manganite heterostructure. *ACS Appl. Mater. Interfaces* **11**, 44837–44843 (2019).
94. Nelson, J. N. et al. Interfacial charge transfer and persistent metallicity of ultrathin $SrIrO_3/SrRuO_3$ heterostructures. *Sci. Adv.* **8**, eabj0481 (2022).
95. Liu, Y. et al. Atomistic origins of surface defects in $CH_3NH_3PbBr_3$ perovskite and their electronic structures. *ACS Nano* **11**, 2060–2065 (2017).
96. Pang, B. et al. Spin-glass-like behavior and topological hall effect in $SrRuO_3/SrIrO_3$ superlattices for oxide spintronics applications. *ACS Appl. Mater. Interfaces* **9**, 3201–3207 (2017).
97. Chen, Y. L. et al. Experimental realization of a three-dimensional topological insulator, Bi_2Te_3. *Science* **325**, 178–181 (2009).
98. Liu, Z. K. et al. A stable three-dimensional topological Dirac semimetal Cd_3As_2. *Nat. Mater.* **13**, 677–681 (2014).
99. Anderson, P. W. Absence of diffusion in certain random lattices. *Phys. Rev.* **109**, 1492–1505 (1958).
100. Kong, D. et al. Rapid surface oxidation as a source of surface degradation factor for Bi_2Se_3. *ACS Nano* **5**, 4698–4703 (2011).
101. Bianchi, M. et al. Coexistence of the topological state and a two-dimensional electron gas on the surface of Bi_2Se_3. *Nat. Commun.* **1**, 128 (2010).
102. Wang, X., Wang, P., Huang, D. & Tan, W. Effects of surface modification on the properties of topological surface states in Bi_2Se_3. *Phys. Lett. A* **376**, 768–772 (2012).
103. Chang, J., Jadaun, P., Register, L. F., Banerjee, S. K. & Sahu, B. Intrinsic and extrinsic perturbations on the topological insulator Bi_2Se_3 surface states. Preprint at https://arxiv.org/abs/1012.2927 (2010).
104. Wray, L. A. et al. Electron dynamics in topological insulator based semiconductor-metal interfaces (topological p-n interface based on Bi_2Se_3 class). Preprint at https://arxiv.org/abs/1105.4794 (2011).
105. Hohenberg, P. & Kohn, W. Inhomogeneous electron gas. *Phys. Rev.* **136**, B864–B871 (1964).
106. Kohn, W. & Sham, L. J. Self-consistent equations including exchange and correlation effects. *Phys. Rev.* **140**, A1133–A1138 (1965).
107. Kresse, G. & Hafner, J. *Abinitio* molecular-dynamics simulation of the liquid-metal-amorphous-semiconductor transition in germanium. *Phys. Rev. B* **49**, 14251–14269 (1994).
108. Kresse, G. & Furthmüller, J. Efficient iterative schemes for *abinitio* total-energy calculations using a plane-wave basis set. *Phys. Rev. B* **54**, 11169–11186 (1996).
109. Perdew, J. P. et al. Restoring the density-gradient expansion for exchange in solids and surfaces. *Phys. Rev. Lett.* **100**, 136406 (2008).
110. Monkhorst, H. J. & Pack, J. D. Special points for Brillouin-zone integrations. *Phys. Rev. B* **13**, 5188–5192 (1976).
111. Mostofi, A. A. et al. Wannier90: a tool for obtaining maximally-localised Wannier functions. *Comput. Phys. Commun.* **178**, 685–699 (2008).
112. Wu, Q., Zhang, S., Song, H.-F., Troyer, M. & Soluyanov, A. A. WannierTools: An open-source software package for novel topological materials. *Comput. Phys. Commun.* **224**, 405–416 (2018).
113. George, C. N. et al. Synthesis and characterization of nanocrystalline strontium titanate through a modified combustion method and its sintering and dielectric properties. *J. Alloy. Compd.* **486**, 711–715 (2009).
114. Yokota, H., Uesu, Y., Malibert, C. & Kiat, J.-M. Second-harmonic generation and x-ray diffraction studies of the pretransitional region and polar phase in relaxor $K_{(1-x)}Li_xTaO_3$. *Phys. Rev. B* **75**, 184113 (2007).
115. Blanchard, P. E. R. et al. Anomalous thermal expansion in orthorhombic perovskite $SrIrO_3$: Interplay between spin-orbit coupling and the crystal lattice. *Phys. Rev. B* **89**, 214106 (2014).

ACKNOWLEDGEMENTS

We are grateful to Hongming Weng, Haizhou Lu, Zhijun Wang, Qihang Liu, Jiachen Gao, and Yuhao Gu for useful discussions and in particular to Andrew Wray for his critical reading of our manuscript. H.C. is supported by the National Natural Science Foundation of China under project number 11774236, the Ministry of Science and Technology of China under project number SQ2020YFE010418, and Open Grant of State Key Laboratory of Low Dimensional Quantum Physics at Tsinghua University. G.L. is supported by NSF of China (Grant No. 11874263), the Sino-German mobility program (M-0006), and Shanghai Technology Innovation Action Plan 2020-Integrated Circuit Technology Support Program (Project No. 20DZ1100605).

AUTHOR CONTRIBUTIONS

H.C. conceived and supervised the project. Z.L. and H.L. contributed equally to this work. Z.L. and H.C. performed the first-principles calculations. G.L. and H.L. performed the model calculations. G.L. refined the focus of the manuscript with H.C. J.M. and X.W. participated in the data analysis. H.C., G.L., Z.L., and H.L. wrote the manuscript.

COMPETING INTERESTS

The authors declare no competing interests.

ADDITIONAL INFORMATION

Supplementary information The online version contains supplementary material available at https://doi.org/10.1038/s41524-022-00894-5.

Correspondence and requests for materials should be addressed to Gang Li or Hanghui Chen.

Reprints and permission information is available at http://www.nature.com/reprints

Publisher's note Springer Nature remains neutral with regard to jurisdictional claims in published maps and institutional affiliations.